metals

MDPI

Article

Effect of Nanostructuring on Operational Properties of 316LVM Steel

Olga Rybalchenko [1], Natalia Anisimova [1,2,3], Natalia Martynenko [1], Georgy Rybalchenko [4], Alexey Tokar [1,3], Elena Lukyanova [1], Dmitry Prosvirnin [1], Mikhail Gorshenkov [3], Mikhail Kiselevskiy [2,3] and Sergey Dobatkin [1,3,*]

[1] A.A. Baikov Institute of Metallurgy and Materials Science, Russian Academy of Sciences, 119334 Moscow, Russia; orybalchenko@imet.ac.ru (O.R.); n.u.anisimova@gmail.com (N.A.); nmartynenko@imet.ac.ru (N.M.); tokar.aa@misis.ru (A.T.); elukyanova@imet.ac.ru (E.L.)
[2] N.N. Blokhin National Medical Research Center of Oncology (N.N. Blokhin NMRCO), Ministry of Health of the Russian Federation, 115478 Moscow, Russia
[3] Institute of Advanced Materials and Nanotechnologies, National University of Science and Technology MISIS, 119049 Moscow, Russia; mvg@misis.ru
[4] P.N. Lebedev Physical Institute, Russian Academy of Sciences, 119991 Moscow, Russia; rybalchenkogv@lebedev.ru
* Correspondence: sdobatkin@imet.ac.ru

Abstract: In this study, high-pressure torsion (HPT) was used to process austenitic 316LVM stainless steel at 20 °C and 400 °C. The effects of HPT on the microstructure, mechanical, and functional properties of the steel were investigated. By applying both HPT modes on the 316LVM steel, a nanocrystalline state with an average size of the structural elements of ~46–50 nm was achieved. The density of the dislocations and twins present in the austenite phase varied depending on the specific HPT conditions. Despite achieving a similar structural state after HPT, the deformation temperatures used has different effects on the mechanical and functional properties of the steel. After HPT at 20 °C, the yield strength of the 316L steel increased by more than nine times up to 1890 MPa, and the fatigue limit by more than two times up to 550 MPa, when compared to its coarse-grained counter-parts. After HPT at 20 °C, the 316LVM steel exhibited better ductility, higher low-cycle fatigue resistance, greater resistance to corrosion, and improved in vitro biocompatibility compared to processing at 400 °C. The reasons for the deterioration of the properties after HPT at 400 °C are discussed in the article.

Keywords: stainless steel; high-pressure torsion; ultrafine-grained microstructure; twinning; mechanical properties; corrosion resistance; biocompatibility in vitro

Citation: Rybalchenko, O.; Anisimova, N.; Martynenko, N.; Rybalchenko, G.; Tokar, A.; Lukyanova, E.; Prosvirnin, D.; Gorshenkov, M.; Kiselevskiy, M.; Dobatkin, S. Effect of Nanostructuring on Operational Properties of 316LVM Steel. *Metals* **2023**, *13*, 1951. https://doi.org/10.3390/met13121951

Academic Editors: Francesca Borgioli, Umberto Prisco, Tomasz Tański and Denis Benasciutti

Received: 1 November 2023
Revised: 22 November 2023
Accepted: 22 November 2023
Published: 28 November 2023

1. Introduction

Austenitic stainless steels (SSs) are widely used in various industrial applications and in the medical field due to their excellent combination of functional properties, including high strength, ductility, corrosion resistance, biocompatibility, and good formability [1]. These materials offer a versatile solution for a range of applications, providing both mechanical and chemical durability. At the same time, they meet the requirements for medical devices and implants [2]. Due to its low carbon content and molybdenum alloying, austenitic 316L stainless steel (SS) exhibits high resistance to various forms of corrosion. Additionally, its high nickel content stabilizes the austenitic phase, resulting in non-magnetic behavior. These properties, combined with its high processability, biocompatibility, and cost effectiveness, make 316L SS an ideal material for the production of internal fixation devices used in orthopedic surgery, as well as for the production of stents used in cardiovascular procedures [3]. The versatile nature of 316L SS allows for its wide application range in both industrial and medical fields. However, SS materials do have

some limitations. For example, they have a low yield strength, which significantly restricts their application range. Additionally, in the field of biomedical usage, one of the lowest fatigue strengths of 316L SS among the alloys used in orthopedics is a disadvantage, since fatigue damage is a common cause of implant failure [4].

It should be noted that stainless steel is predominantly used for manufacturing implantable devices for osteosynthesis. Some of them have increased strength requirements. Thus, for skeletal pins made of deformable stainless steel with dimensions from 1 to 2.8 mm, the tensile strength should be at least 1240 MPa with a minimum elongation of about 3% [5]. Since surgical grade 316L SS is a stable material that does not undergo phase transformations during heat treatment and deformation, grain refinement is one of the few strategies used to increase the strength [6]. Among the effective methods of grain refinement is severe plastic deformation (SPD) [7,8]. Studies [9–13] have demonstrated improvements in the mechanical and operational properties, including fatigue strength, by obtaining an ultrafine-grained (UFG) structure in austenitic corrosion-resistant steels through equal channel angular pressing (ECAP) method. Another promising method that allows the ultrafine structure refinement without steel sample destruction is high-pressure torsion (HPT) [8,14–18]. This method has already been tested on austenitic stainless steels, including 316L SS [19–31].

All studies confirmed the achievement of a nanocrystalline state in 316L SS after HPT. Thus, in [21], a grain refinement up to 50 nm was noted during high-pressure torsion at 10 revolutions. Researchers [21] have also highlighted the occurrence of a martensitic $\gamma \rightarrow \varepsilon \rightarrow \alpha'$ transformation in the steel structure during HPT, which has resulted in a significant increase in hardness up to 6000 MPa. Furthermore, it has been noted that hardness is more sensitive to changes in grain size rather than changes in phase composition. On the contrary, in the study of the deformation mechanisms through HPT in 316L steel over a wide temperature range from −196 °C up to 720 °C, Scheriau et al. [22] determined that only at deformation temperatures below room temperature does the deformation-induced γ (fcc) $\rightarrow$ ε (hcp) transformation occur. At deformation temperatures above 450 °C, the dominant mechanism was dislocation slip, while in the range below 450 °C to room temperature, deformation twinning in the austenite phase was observed. At the same time, the authors in [22] noted a refinement of the average grain size to 100 nm after HPT at room temperature. Moreover, in many studies, authors have noted the increase in hardness both after the post-deformation annealing of 316L SS [23–26] and during deformation through HPT at elevated temperatures [26].

Wang et al. [23] investigated nanocrystalline plates of 316L stainless steel in the annealed austenitic state obtained through HPT at 500 °C for one hour using TEM analysis and specific electrical resistivity measurements. Thus, the study [23] concluded that the strengthening of 316L SS occurred through a combination of nanostructuring during HPT and the precipitation of segregations during annealing. The authors in their work made a comparative analysis of the mechanical characteristics of steel 316L. At that time, their results were the most impressive. The tensile strength of the samples subjected to HPT was 1790 ± 50 MPa and further increased with increasing annealing temperature to 500 °C, reaching a maximum value of 2390 ± 50 MPa.

In further research, Renk et al. [24,25] confirmed the precipitation of segregations in samples of 316L SS with a diameter of 35 mm and a height of 11 mm. The samples were nanostructured using the quasi-constrained high-pressure torsion method under a pressure of 3.60 GPa for 15 rotations. In the study [23], the authors demonstrated a 20% increase in the hardness of nanostructured 316L SS after annealing at 823 K for 30 min. After comparing the results of mechanical testing and atom probe tomography (APT) data, it was concluded that the increase in the hardness of 316L SS was not caused by segregations of dissolved elements. However, the particles of dissolved elements or second phases stabilize the nanocrystalline structure. Therefore, they allow for annealing processes such as annihilation and relaxation, which are necessary for strengthening phenomena during annealing. These particles play a role in maintaining the stability and enhancing

the mechanical properties of the nanocrystalline material. In a subsequent study [25], the same authors attempted to improve the fatigue limit of 316L SS by annealing it at 823 K for 90 min, since this treatment resulted in the greatest increase in strengthening. They noted that the strain strength of 316L SS after 15 turns of quasi-constrained high-pressure torsion was 1865 MPa, which increased to 2226 MPa after annealing. During the experiment, the fatigue limit increased up to 1 GPa. The authors concluded that the reason for the increase was due to defect relaxation, which shifted the onset of plasticity to higher stress levels, combined with the stabilization of nanograin boundaries through segregations.

In the study [26], 316 steel was nanostructured using the HPT method at room temperature and at 400 °C. As a result, after applying HPT to the austenitic steel at different temperatures, an ultrafine-grained structure was obtained. This was characterized by different dislocation and twinning densities, different grain sizes of 40 and 90 nm at room temperature and at 400 °C, respectively, while demonstrating a similar level of increased strength of approximately 1700 MPa. Furthermore, the use of atom probe tomography (APT) revealed that HPT at elevated temperatures resulted in the formation of Mo–Cr–Si segregations in 316 stainless steel. Taking into account the various contributions to the material strengthening, the authors demonstrated that segregations could lead to a significant increase in strength. By impeding the dislocation glide, segregations also enhance the yield strength. Since the initiation of fatigue cracks is a result of dislocation glide, HPT at 400 °C is expected to result in a significant increase in the fatigue limit.

The aim of this study was to investigate the effect of HPT nanostructuring at two temperatures, room temperature and 400 °C, on the operational characteristics of surgical grade 316LVM stainless steel, including fatigue strength, corrosion resistance, and in vitro biocompatibility. It is expected that the high specific strength of 316LVM stainless steel after HPT will make it possible to decrease the size of implants and, as a result, reduce the toxic effect of the implanted device on the human body The promising results in [26] raised hopes for obtaining not only a high specific strength of surgical grade steel after HPT at 400 °C but also fatigue strength while maintaining or even improving corrosion resistance and in vitro biocompatibility.

2. Materials and Methods

The study utilized an austenitic 316LVM stainless steel with low carbon content, which is commonly used for implant manufacturing. The nominal composition of the 316LVM steel is presented in Table 1. The material was initially in the as-received state and was solution treated at 1050 °C for 1 h, followed by being quenched in water (solution heat treatment). High-pressure torsion (HPT) deformation was conducted using a Bridgman-type setup (JEOl, Tokyo, Japan) on samples with a diameter of 20 mm and a thickness of 1.5 mm, applying a pressure of 6 GPa. HPT was performed using two isothermal deformation modes: at temperatures of 20 °C and 400 °C. For all deformation modes, the samples were subjected to 10 rotations, which corresponds to a true strain of approximately 5.7 at the center of the sample radius.

Table 1. Chemical composition of the 316LVM stainless steel.

Elements	Amount (wt.%)									
	C	**Cr**	**Ni**	**Cu**	**Si**	**Mn**	**Mo**	**N**	**S, P**	**Fe**
316LVM	0.012	17.3	14.11	0.07	0.24	1.77	2.75	0.07	0.001/0.024	balance

TEM analysis of the structure was conducted using a JEM-200CX microscope (JEOl, Tokyo, Japan), while the X-ray diffraction (XRD) analysis was performed using a DRON 4.07 diffractometer in the 2θ angle range from 10 to 130° at a scanning step value 0.1° with CoKα radiation (wave length: λ = 1.7902 Å) at rated operation X-ray sources of 60 kV and focus size of 1.0 mm × 10 mm.

For the foils, samples were taken from the middle of the sample radius. Microhardness measurements were conducted using a 402 MVD Wolpert Wilson instrument with a 1 N load. Mechanical properties were determined using an "INSTRON 3382" machine (INSTRON, Norwood, MA, USA) on flat samples that were 1.0 mm thick, 1.0 mm wide, and had a working length of 2.0 mm (Figure 1), in accordance with [32]. High-cycle fatigue tests were performed under repeated tension conditions on an INSTRON 8801 servo-hydraulic machine with a maximum load capacity of 100 kN, a testing frequency of 40 Hz, and a stress ratio of R = 0.1 on flat samples 1.0 mm thick, 1.0 mm wide, and with a length of the working part of 1.6 mm.

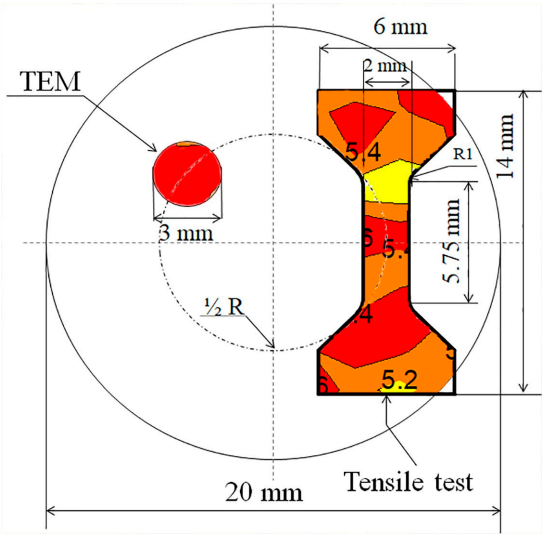

Figure 1. Schematic representation showing the locations of all investigation and test samples on the HPT disk. Red, orange, and yellow colors indicate different levels of microhardness. Thus, it is noted that we used the distribution of microhardness values over the surface for choosing the place to cut the samples for testing. The sample was cut from the area with uniform deformation.

Corrosion potential, corrosion current density, and corrosion rate were evaluated from the results of electrochemical tests by the potentiodynamic polarization (PDP) method using an SP-300 potentiostat (Bio-Logic SAS; Seyssinet-Pariset, France). They were obtained using EC-Lab software (BioLogic, Seyssinet-Pariset, France), in accordance with [33]. Corrosion studies were carried out in physiological solution at room temperature. A flat cell with a "three-electrode configuration" with the test sample as the working electrode was used. The Ag/AgCl electrode (with 3 M NaCl electrolyte inside) and platinum grid were the reference and counter electrodes, respectively. The area exposed to the solution was about 1 cm^2. Scanning was performed at a rate of 1 mV/s in the scanning range: −1.50 V vs. E_{OC}; +0.700 V, where E_{OC} is the open circuit potential. The time for determining the open circuit potential was 60 min.

To assess the impact of HPT processing on the biocompatibility of 316LVM SS, the level of hemolysis and cytotoxicity relative to non-transformed immunocompetent blood cells was evaluated. For the evaluation of hemolytic activity, the 316LVM steel samples were incubated in 2 mL of Hank's solution containing 14.8×10^6 human erythrocytes at 37 °C in an atmosphere with 5% carbon dioxide. The incubation was carried out for 2, 4, and 24 h. The level of hemolysis was determined according to a previously described method [34].

To study cytotoxicity, the steel samples were incubated in 2 mL of complete growth medium containing 540,000 mononuclear leukocytes isolated from the venous blood of a healthy donor using a Ficoll gradient. The incubation was performed at 37 °C in an atmosphere containing 5% carbon dioxide for 24 h. In the control group, cells were incubated in complete growth medium under the same conditions. The influence of the steel on

tumor cell viability was assessed by calculating the ratio of cell activity on the surface of the samples to the control in the MTT assay, as described previously [35].

For cell colonization experiments, a human MMSC culture from the cell culture collection of the N.N. Blokhin National Medical Research Center of Oncology consisting of 20,000 cells was applied to the surface of the alloy samples after forging and after HPT, with a volume of 15 µL. The samples were incubated for 30 min at 37 °C in an atmosphere with 5% carbon dioxide. After incubation, 1 mL of complete growth medium was added to the samples containing cells, and they were then incubated for 21 days under the same conditions. In the control group, cells were incubated on the bottom of the well plate under the same conditions. The growth medium was changed every 2 days.

Cell colonization was studied using fluorescence microscopy with a LionHeart LX digital microscope (Perkin Elmer, Waltham, MA, USA) after staining the cells with Calcein AM (Sigma, St. Louis, MO, USA) following the manufacturer's instructions. At the end of the experiment, the alloy samples were removed from the well plate in which incubation took place and treated with 1 mL of trypsin. In the control group, the growth medium was removed and the cells were treated with trypsin. Cell viability was assessed using The Muse Count & Viability Kit (Muse, Thermo Scientific, Waltham, MA, USA) and the Muse cell analyzer (Millipore, Darmstadt, Germany). To study the expression of adhesion molecules by the cells, they were stained with antibodies against CD44 (BD Bioscience, San Diego, CA 92121, USA) and CD11b (BD Bioscience, San Diego, CA, USA), and the number of CD44(+), CD11b(+), and CD44(+)CD11b(+) cells was determined using a NovoCyte flow cytometer (ACEA Bioscience Inc., San Diego, CA 92121, USA) based on the analysis of at least 10,000 cells in the sample.

The results of the research were presented as the mean value and standard deviation (mean ± SD). In order to perform comparative analysis with the control groups, a *t*-test was used. Differences were considered statistically significant at $p < 0.05$. The experiments and procedures with cells and animals were assessed and approved by the Local Ethics Committee of "N.N. Blokhin National Medical Research Center of Oncology" of the Health Ministry of Russia (#8-03, 1 March 2023).

3. Results

3.1. Microstructural Characterization of the 316LVM Stainless Steel in the Initial State and after HPT

Figure 2 shows the initial structure of the 316LVM stainless steel in the forged state (Figure 2a) and after solution heat treatment (Figure 2b).

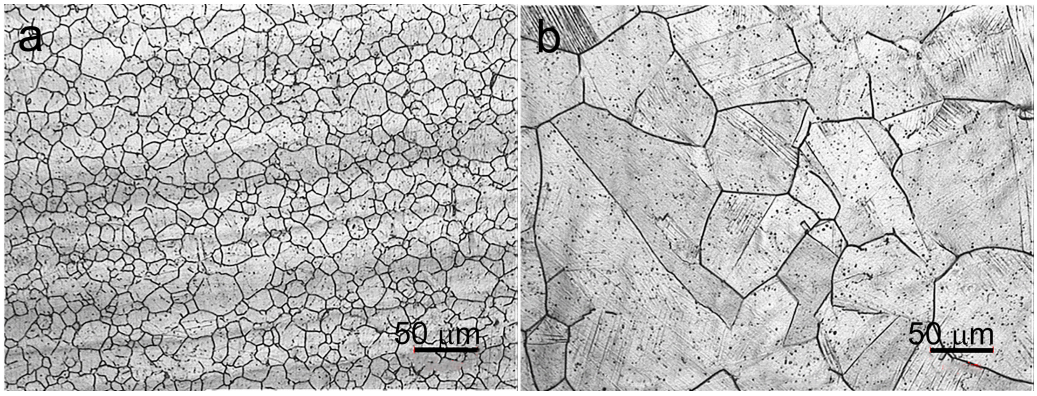

Figure 2. Optical micrographs of the 316LVM stainless steel after forging (**a**) and solution heat treatment (**b**).

After HPT at room temperature and at 400 °C, a nanocrystalline structure with predominantly high-angle grain boundaries is formed in the 316LVM steel (Figure 3). The presence of a grain structure was determined by the circular electron diffraction pattern with point reflections. HPT at room temperature resulted in a microstructure, with an

average size of the structural elements of about 46 ± 1.8 nm and deformation twins in the austenitic matrix (Figure 3a,b). With an increase in the HPT temperature up to 400 °C, the character of the forming structure remains the same, and the average size of the structural elements increases slightly to 50 ± 1.6 nm (Figure 3c,d). Moreover, the density of twins after HPT at 400 °C, according to the TEM analysis (Figure 3b,d), is four times higher than at 20 °C. Deformation twinning typically occurs when slip is hindered for various reasons.

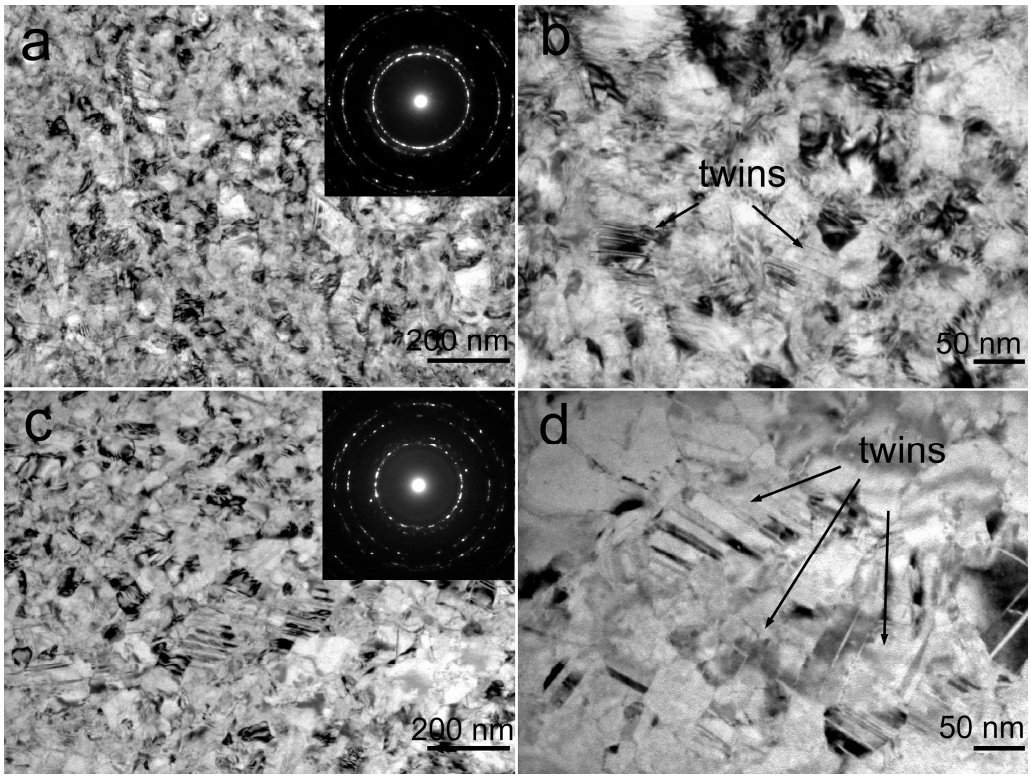

Figure 3. TEM images of the 316LVM stainless steel after HPT at 20 °C (**a**,**b**) and 400 °C, (**c**,**d**) with SAED pattern seen in the inset of (**a**,**c**).

3.2. X-ray Analysis of the 316LVM Stainless Steel after HPT

The X-ray structural quantitative phase analysis revealed the presence of a fully austenitic structure in the steel, deformed under all processing regimes (Figure 4, Table 2). By analyzing the width of the X-ray lines of the austenite (111) and (222) reflections, the parameters of the fine crystalline structure of the 316LVM stainless steel after HPT were determined (Table 3). This included the crystallite size (d) and the root mean square microstrain, which further allowed for the calculation of the dislocation density (Table 3). The line profiles were fitted using Gaussian functions. The X-ray structural analysis did not reveal any significant differences in the sizes of the CSRs (30–40 nm) and showed a twofold decrease in the dislocation density after increasing the deformation temperature from room temperature to 400 °C. The values of microstrains decrease with an increase in the HPT temperature. The highest value of microstrain was obtained after HPT at room temperature. The decrease in the CSR values corresponds to a reduction in the grain size observed through the electron microscopy analysis. However, there is only a slight difference between the average size of the structural elements determined by electron microscopy and the CSR size determined by the X-ray structural analysis. This discrepancy may be attributed to the fact that X-ray structural analysis takes into account subgrain structures that are not always detectable through electron microscopy [36].

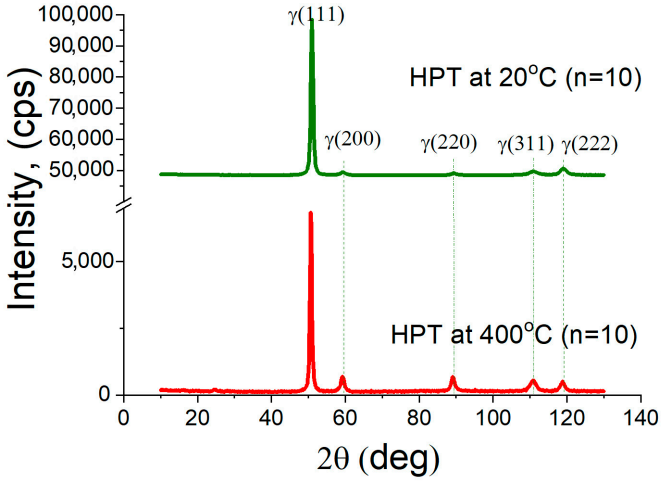

Figure 4. XRD patterns of the 316LVM stainless steel after HPT (n—number of revolutions).

Table 2. Results of the X-ray phase analysis of the 316LVM stainless steel after HPT.

Processing	Space Group	Phase	a, Å	Content, wt.%
HPT, at 20 °C	225: Fm-3m	γ	3.596	100.0 ± 0.0
HPT, at 400 °C	225: Fm-3m	γ	3.599	100.0 ± 0.0

Table 3. Crystallite size, microstrain, and dislocation density of the 316LVM stainless steel after HPT determined by X-ray line profile analysis.

Processing	β_{111}, °	β_{222}, °	d, nm [1]	ε, % [2]	ρ, 10^{15} (m^{-2}) [3]
HPT, at 20 °C	0.82 ± 0.08	2.56 ± 0.25	31.4 ± 1.52	0.33 ± 0.10	143.2
HPT, at 400 °C	0.60 ± 0.06	1.83 ± 0.18	41.5 ± 1.89	0.23 ± 0.07	75.4

[1] d—crystallite size, [2] ε—microstrain, [3] ρ—dislocation density.

3.3. Microhardness of the 316LVM Stainless Steel after HPT

The degree of deformation during HPT increases with the distance from the center along the radius, resulting in smaller sizes of the structural elements towards the edge of the sample and higher microhardness values. All investigated samples after HPT exhibited lower microhardness values in the center of the sample (4.2–5.0 GPa) and an increase in microhardness at the edge of the sample, reaching 5.0–5.5 GPa (Figure 5a). The samples subjected to HPT at room temperature showed more uniform deformation with the smallest difference in microhardness between the center and the edge of the sample.

Figure 5 illustrates the distribution of microhardness over the surface of an HPT sample after HPT from the side of the plunger (Figure 5b,d) and support (Figure 5c,e). The microhardness values from the support side are higher and more uniformly distributed across the surface. The microhardness measurements across the sample surface visually demonstrated not only a significant difference in the microhardness values between the center and edges of the samples after HPT at 400 °C, but also higher microhardness values in these samples at the established stage with the same microhardness (1/2 R—R from the center of the sample).

The investigation of the thermal stability of the steel samples after severe plastic deformation (SPD) revealed that the deformation strengthening for all modes decreases at temperatures above six hundred and fifty degrees due to grain growth (Figure 6). In the temperature range of 400–650 °C, there is a slight increase in microhardness, with the growth in microhardness starting slightly earlier and being more pronounced at a deformation temperature of 400 °C.

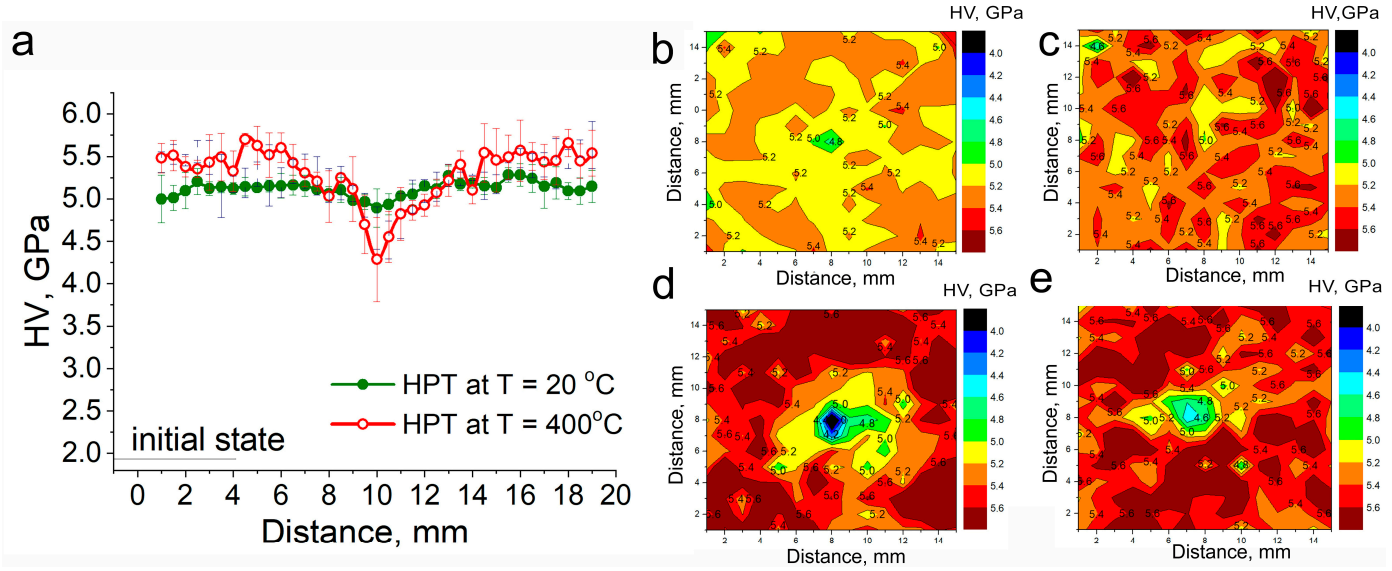

Figure 5. Microhardness of the 316LVM stainless steel produced by HPT: (**a**) along the diameter; (**b**–**d**) distribution over surface of an HPT sample after HPT at 20 °C (**b**,**c**) and after HPT at 400 °C (**d**,**e**); from the side of the plunger (**b**,**d**) and support (**c**,**e**).

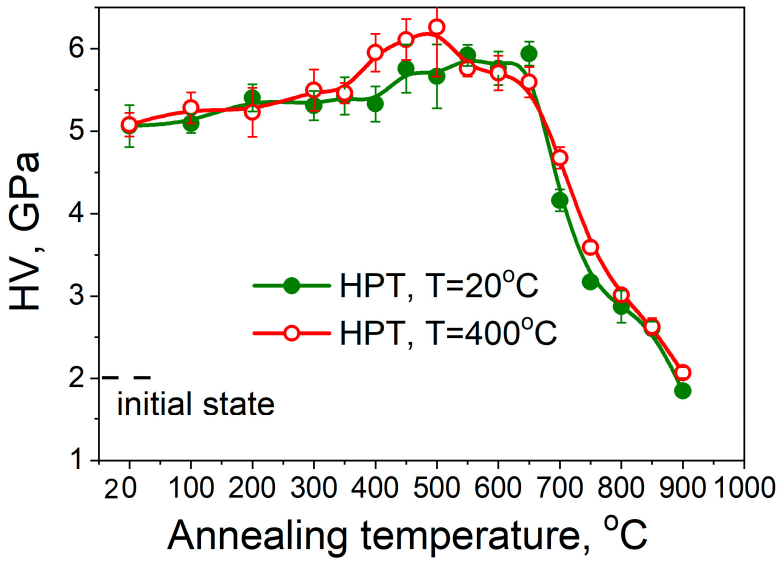

Figure 6. Microhardness of the 316LVM stainless steel produced by HPT as a function of annealing temperature.

3.4. Mechanical Properties under Static and Cyclic Loading

HPT significantly enhances the strength characteristics of the 316LVM steel (Figure 7, Table 4). The yield strength increases by more than nine times, while the ultimate tensile strength increases by four times. However, the ductility decreases after HPT at 20 °C to $\varepsilon = 11\%$, and sharply drops to $\varepsilon = 1\%$ at a deformation temperature of 400 °C. At approximately similar average sizes of the structural elements, an increase in the HPT temperature results in a twofold decrease in the density of free dislocations and an increase in the density of twins, which should not lead to a loss of ductility compared to the deformation level at room temperature.

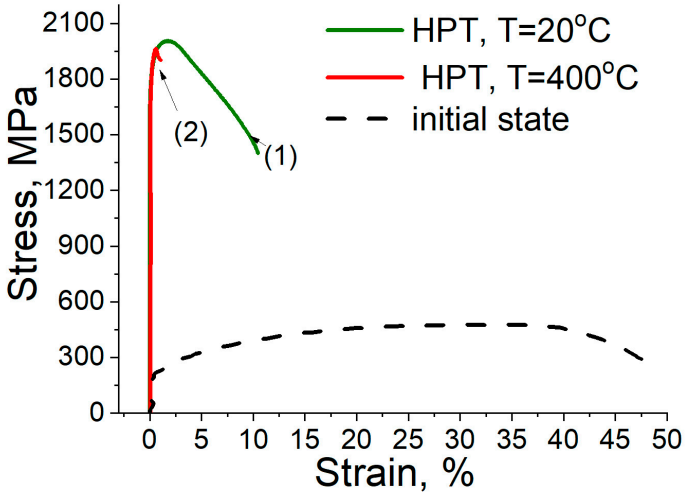

Figure 7. Stress–strain curves of the 316LVM stainless steel after solution heat treatment and HPT.

Table 4. Mechanical properties of the 316LVM stainless steel after solution heat treatment and HPT.

Processing	σ_{UTS} [MPa] [1]	σ_{YS} [MPa] [2]	ε [%] [3]
HPT, at 20 °C	2005 ± 24	1890 ± 6	11 ± 0.45
HPT, at 400 °C	1960± 18	1820 ± 12	1 ± 0.3
Quenching	500 ± 4	200 ± 6.5	47.6 ± 1.5

[1] Ultimate tensile strength; [2] yield strength; [3] total elongation.

The fatigue limit of the samples after HPT at room temperature (550 MPa) exceeds the fatigue limit of the as-quenched sample (250 MPa) by more than twofold (Figure 8). Previously, the authors of this study observed a significant increase in the fatigue strength due to grain refinement and twinning in austenite during severe plastic deformation (SPD) and subsequent cyclic deformation [13].

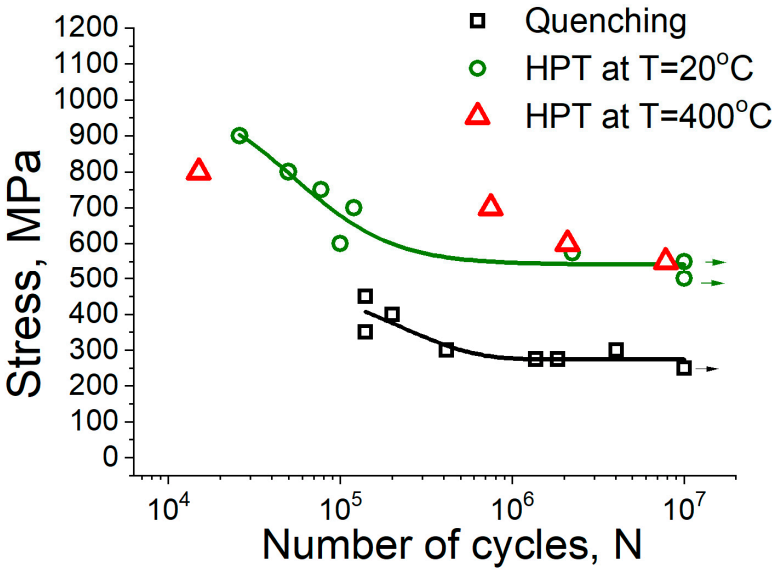

Figure 8. The Woehler (S-N) curves for cyclic deformation of the 316LMV stainless steel after solution heat treatment and HPT.

The results of the study on the samples after HPT at 400 °C did not reveal a decrease in high-cycle fatigue, but showed a slight decrease in stress under low-cycle loading compared to the samples after HPT at 20 °C.

The fractography of the surface of the as-quenched sample after fatigue failure indicates that, in the fatigue crack initiation and propagation zone (Figure 9a), a predominantly ductile nature of the surface relief is observed. In certain areas, the relief appears quasi-ductile with signs of fatigue striations (Figure 9b). In static fractures, typical ductile dimple fractures are observed (Figure 9).

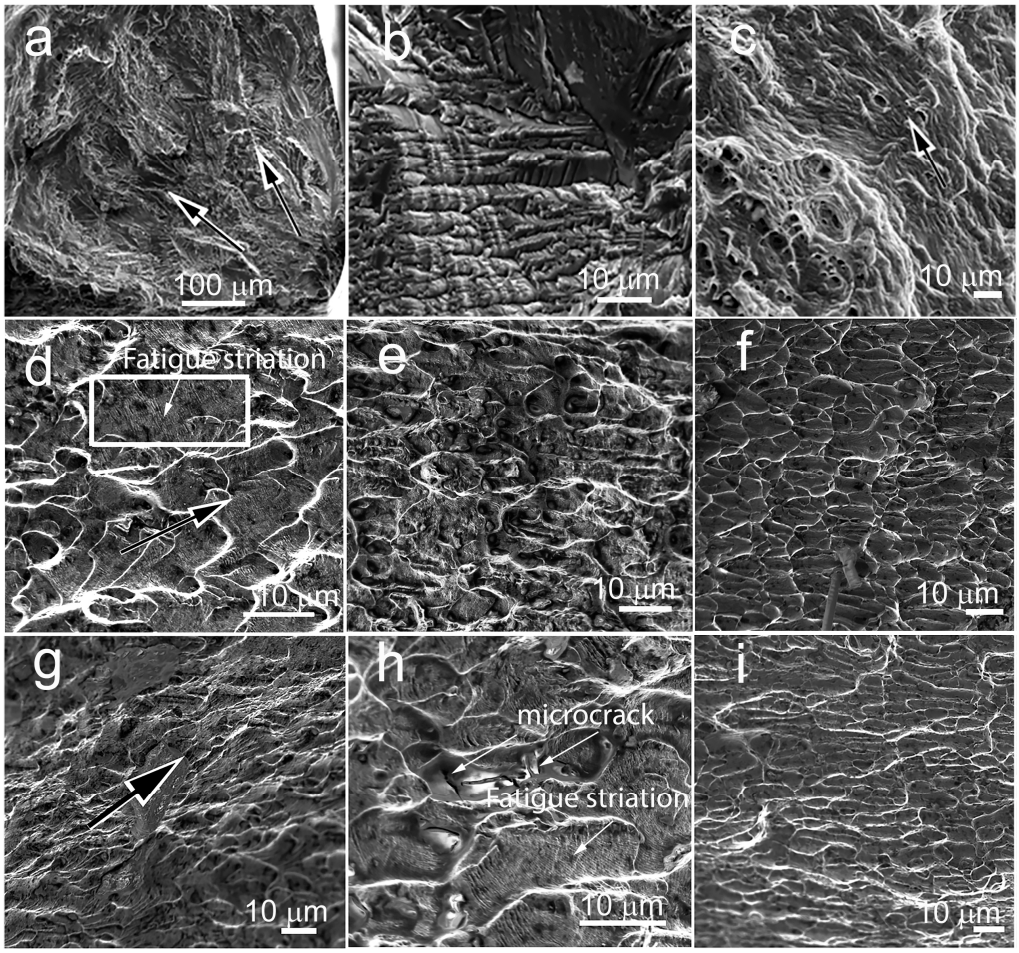

Figure 9. Fracture surfaces of fatigue failure of the 316LVM stainless steel samples after solution heat treatment (**a**–**c**), HPT at RT (**d**–**f**) and HPT at 400 °C (**g**–**i**).

After HPT, the relief in the fatigue crack initiation and propagation zone is less developed compared to the case of samples in the as-quenched state. A distinct zone of accelerated crack growth before the static fracture can be clearly identified (Figure 9d,g). The main crack propagation direction along the striations is shown at the figures. Signs of fatigue striations are observed (Figure 9d,h). The static fracture, as in the as-quenched samples, is associated with a ductile dimple fracture mechanism (Figure 9f,i). Deeper dimples on the fracture surface of the sample after HPT at room temperature indicate higher material ductility compared to the samples after HPT at 400 °C. The presence of microcracks within the dimples (Figure 9h) after HPT at 400 °C suggests the presence of grain boundary precipitates, which could have contributed to their initiation.

3.5. Corrosion Resistance of the 316LVM Stainless Steel in the Initial State and after HPT

The results of the potentiodynamic analysis on the 316LMV stainless steel samples in the as-quenched state and after HPT are presented in Figure 10. HPT at room temperature, based on the polarization curves, shows minimal changes in the corrosion resistance (Figure 10a).

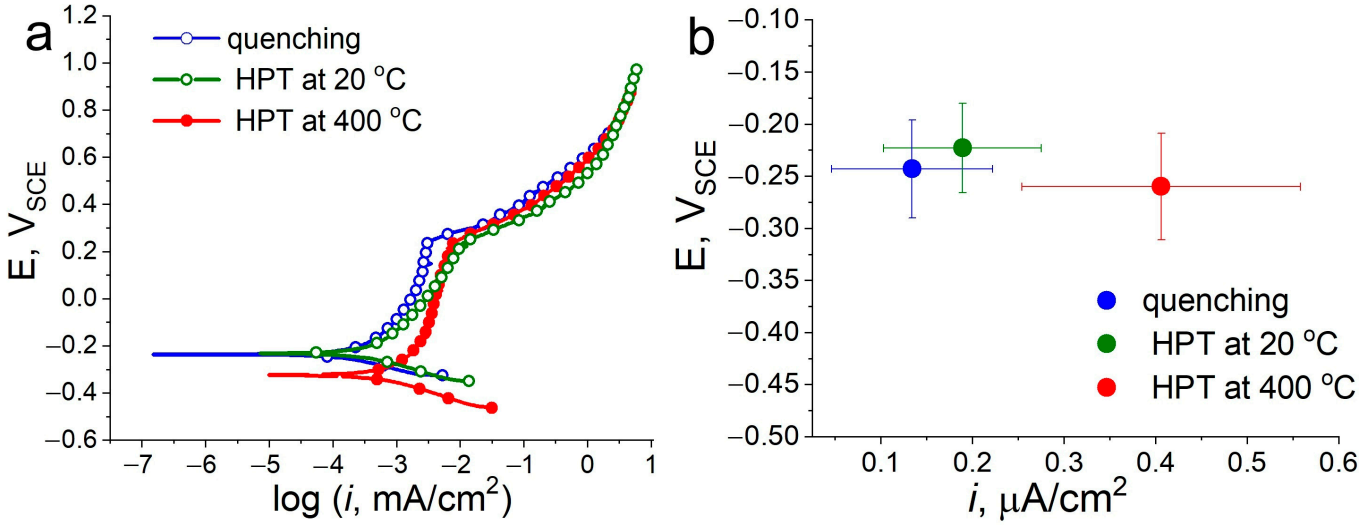

Figure 10. PDP curves in 0.1 M NaCl (pH = 6) electrolytes at scan rate of 1 mV/s (**a**) and E vs. corrosion current density (*i*) (**b**).

The lower corrosion potential (E_{corr} = −260 ± 51 mV) and higher corrosion current density (i_{corr} = 0.406 ± 0.152 μA/cm^2) compared to the as-quenched state (E_{corr} = −243 ± 47 mV, i_{corr} = 0.134 ± 0.088 μA/cm^2) and the state after HPT at 20 °C (E_{corr} = −223 ± 48 mV, i_{corr} = 0.189 ± 0.081 μA/cm^2) indicate a lower corrosion resistance of the samples after HPT at 400 °C (Figure 10b, Table 5).

Table 5. Potentiodynamic polarization parameters of the 316LVM stainless steel.

Processing	E_{corr} [1], mV	i_{corr} [2], μA/cm^2
Quenching, at 1050 °C (1 h)	−243 ± 47	0.134 ± 0.088
HPT at 20 °C	−223 ± 48	0.189 ± 0.081
HPT at 400 °C	−260 ± 51	0.406 ± 0.152

[1] Corrosion potential; [2] corrosion current density.

3.6. Biocompatibility In Vitro of the 316LVM Stainless Steel in the Initial State and after HPT

In order to assess the effect of deformation using the HPT method on the biocompatibility of the 316LVM stainless steel, the hemolysis levels were examined after incubation with the samples, as well as their cytotoxicity relative to non-transformed immune-competent blood cells. It is important to note that, in this study, materials are considered biocompatible with low hemolytic activity if they induce a degree of hemolysis of no more than 5%, in accordance with recommendations [37]. The hemolysis levels were evaluated after 2, 4, and 24 h of incubation relative to the spontaneous hemolysis level in the control with intact cells.

The conducted studies showed that the hemolytic activity of all the examined samples did not exceed 2% throughout the entire observation period (Figure 11a). Furthermore, no significant difference in the impact on the hemolysis level was observed between the alloy in its as-received state and after HPT.

The assessment of the cytotoxicity of the steel (Figure 11b) through measuring the level of cell activity using the MTT (3-[4,5-dimethylthiazol-2-yl]-2,5 diphenyl tetrazolium bromide) assay after 1 day of incubation, relative to the control with intact cells, was performed. The results showed that the presence of the examined samples, both in their as- quenched state and after HPT, did not lead to a significant change in cell activity level ($p > 0.05$). Thus, no signs of the cytotoxic effects of the 316LVM SS were found in this cell model.

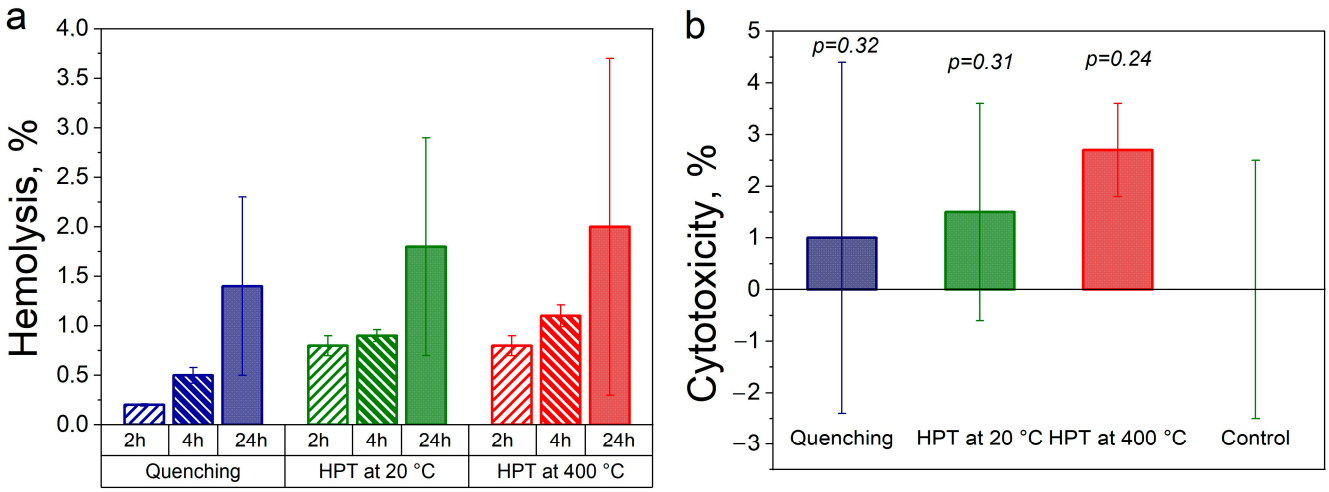

Figure 11. The hemolysis (**a**) and cytotoxicity (**b**) of the 316LVM stainless steel samples after solution heat treatment and HPT calculated as a percentage relative to control.

Since the examined samples of the 316LVM SS in their as-quenched state and after HPT did not induce hemolysis exceeding 2% and did not exhibit cytotoxicity, these samples can be considered biocompatible. HPT did not lead to a significant deterioration in this parameter.

In order to investigate the impact of the processing of the 316LVM SS on the colonization of mesenchymal stromal/stem cells (MSCs), the cells were incubated on the surface of the samples in their as-quenched state, after HPT at room temperature, and after HPT at 400 °C for a period of 21 days. The assessment of their viability on the surface of the samples did not reveal any significant differences in the proportion of viable cells compared to the control ($p < 0.05$) on the surface of the samples in their as-quenched state and after HPT at 20 °C (Figure 12). However, on the surface of the samples after HPT at 400 °C, there was a 1.2-fold decrease in the concentration of adhered viable cells compared to the control ($p = 0.04$).

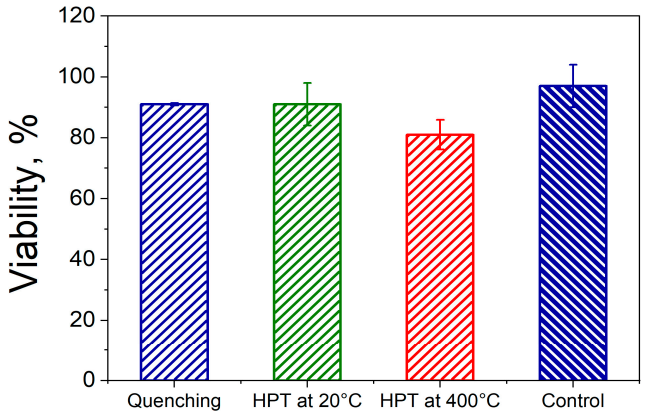

Figure 12. Cell viability on the surface of the 316LVM stainless steel samples after solution heat treatment and HPT relative to control.

The images allowing for the evaluation of the number of live and dead cells colonizing the 316LVM SS samples at the end of the incubation period indicate not only a decrease in the ratio of live/dead cells on the surface of the 316LVM SS sample after HPT at 400 °C but also a suppression of cellular colonization overall (Figure 13). It is important to note that the concentration of live cells on the surface of the 316LVM SS samples after HPT at 20 °C was approximately comparable to or even slightly higher than that of the as-quenched state sample. At the same time, it was observed that the majority of cells were not arranged

individually but rather in groups, forming colonies. This can be interpreted as evidence of an actively ongoing cell division process, accompanying the colonization of the surface of the samples.

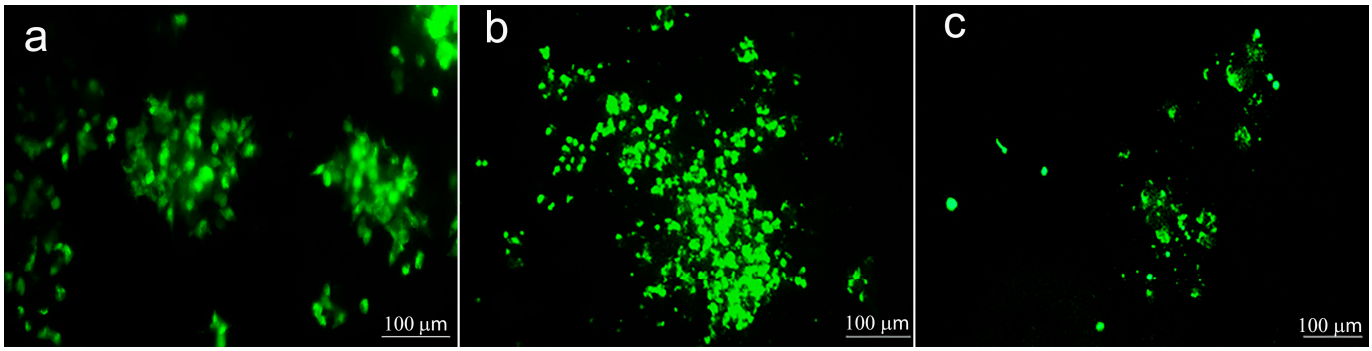

Figure 13. Surface colonization of the 316LVM stainless steel samples after solution heat treatment (**a**), HPT at 20 °C (**b**), and HPT at 400 °C (**c**) by MMSC after 21 days of incubation. Cell staining Calcein AM.

The next step was to further investigate the mechanism underlying the observed effect of 316LVM SS processing on the cell colonization. In order to do this, the change in the concentration of cells expressing the adhesion molecules CD11b and CD44 on the cell membranes, colonizing the surface of the steel, was studied in comparison to the control (Figure 14). The transmembrane molecules of integrin CD11b are involved in various aspects of cellular activity and influence cell attachment to the extracellular matrix. The transmembrane glycoprotein molecules CD44, integrated into the cell membrane, influence both cell adhesion to the extracellular matrix and intercellular interactions, promoting cell migration.

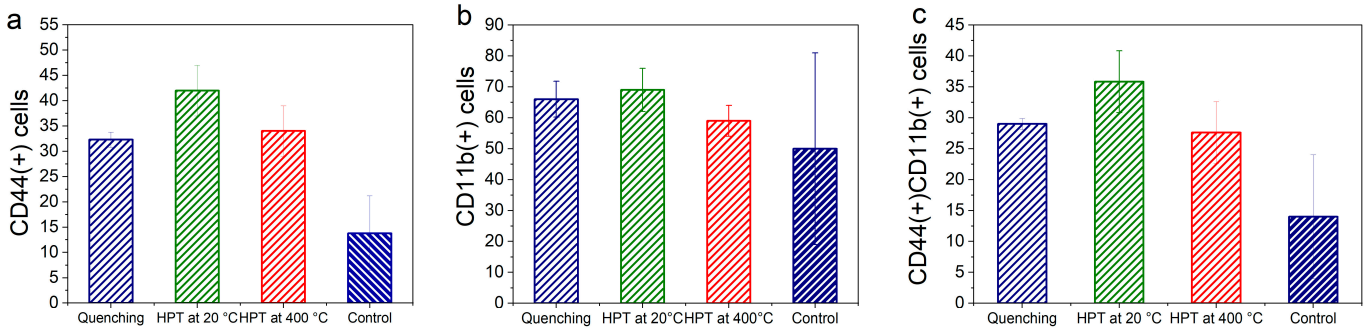

Figure 14. The expression of adhesion molecules CD44 and CD11b on the membranes of MSCs colonizing the surface of the 316LVM SS samples in the initial state and after HPT was compared to the control.

According to the obtained data, contact with the 316LVM SS samples stimulated the expression of the surface adhesion molecules CD44 and CD11b in MSCs compared to the control. Moreover, the impact of 316LVM SS after HPT at 20 °C was more pronounced compared to the as-quenched sample and the sample after HPT at 400 °C. This effect was determined to a lesser extent by an increase in the expression of CD11b integrins on the cell surface and, to a greater extent, by an increase in the expression of CD44. Thus, it can be concluded that the cell colonization of the 316LVM SS samples was caused by the stimulation of synthesis and expression of transmembrane adhesion molecules by the cells. Moreover, the samples after HPT at 20 °C stimulated colonization to the greatest extent through the involvement of this mechanism.

4. Discussion

In this study, surgical grade 316LVM stainless steel was investigated, which undergoes vacuum arc remelting in order to increase its purity (lower phosphorus and sulfur content), making it more corrosion-resistant and biocompatible compared to 316L. The chemical composition of 316LVM stainless steel differs slightly from 316L. It has an increased lower limit for molybdenum, reduced silicon content (maximum allowable value of 0.75% vs. 1.0%), and a higher range for allowable chromium and nickel content according to [38]. In addition, the microstructure should not contain molybdenum-enriched chi and sigma intermetallic compounds, which can reduce corrosion resistance and potential embrittlement.

In this study, two HPT modes, performed at room temperature and at 400 °C, resulted in a nanocrystalline state in the 316LVM steel, with an average size of the structural elements of 46 ± 1.8 nm and 50 ± 1.6 nm, respectively. The structure differed only in the density of the twinning in the austenite (four times higher after HPT at 400 °C, as observed using TEM) and the density of the dislocations (twice higher after HPT at 20 °C, as measured by X-ray). No precipitates were detected in the microstructure of the 316LVM steel using TEM. The above-mentioned distinguishing features of the microstructure do not explain the similar levels of strength properties with a significant difference in ductility between the two states after HPT at room temperature and at 400 °C (ε = 11 ± 0.45% and ε = 1 ± 0.3%, respectively). Only the increased density of twins indicates that something hindered the dislocation glide during the HPT process at 400 °C.

When comparing with the above data from the literature, it should be noted that in this work, after HPT at 20 °C, higher strength characteristics were obtained (σ_{UTS} = 2005 ± 24 MPa) with satisfactory ductility (ε = 11%). At the same time, the best result of the ultimate strength presented in the literature was achieved in [25] and amounted to 1865 MPa. This result was obtained after quasi-constrained high-pressure torsion under pressure for 15 revolutions. After 10 revolutions of HPT in [23], the tensile strength was about 1790 ± 50 MPa. The same amount of revolutions in the case of the paper presented here resulted in a higher level of strength and can be explained by a greater grain refinement, 46 ± 1.8 nm versus 62 nm, in [23]. However, subsequent annealing after HPT led to a further increase in strength to 2390 MPa in [23] and to 2226 MPa in [25]. This increase in strength after annealing was accompanied by a significant increase in fatigue strength up to 1 GPa. In this work, heating during HPT did not increase the strength of the steel compared to HPT at room temperature, but only worsened the ductility.

The mechanism reported in [22–25] of the segregation of Mo–Cr–Si precipitation, allow us to suppose that the increased content of Mo and Cr in the investigated 316LVM steel could have led to more pronounced segregation. This had a negative impact not only on the mechanical properties (Figure 7, Table 4) but also on the operational characteristics. The results of the fatigue tests showed a decrease in fatigue strength under low-cycle loading (Figure 8). Moreover, the fractographic analysis of the fracture surface of the sample after HPT at 400 °C revealed the presence of microcracks (Figure 9h), indicating possible segregation that could have been the cause of their initiation. The corrosion studies using potentiodynamic polarization analysis revealed that HPT at 400 °C reduces the corrosion potential of the surgical steel, and increases the corrosion current density of the samples (Figure 10, Table 5). The in vitro studies (Figures 11–14) of the 316LVM stainless steel revealed lower biocompatibility indicators for samples after HPT at 400 °C. However, while the difference in the hemolysis and cytotoxicity levels of the samples (Figure 11) was not significant ($p > 0.05$), the colonization of the MMSCs on the surface of the steel after HPT at 400 °C (Figure 12) showed a decrease in the concentration of adhered living cells compared to the control ($p = 0.04$). Additionally, there was an overall suppression of cell colonization (Figure 13).

Thus, this study has established that the previously observed segregation of Mo–Cr–Si in 316L stainless steel can significantly deteriorate the operational characteristics in surgical

grade 316LVM steel with higher Mo and Cr content, negating the advantages of its high-strength state.

Simultaneously, the 316LVM SS samples after HPT at 20 °C demonstrated a high combination of properties. Not only were high strength characteristics observed (σ_{UTS} = 2005 MPa and σ_{YS} = 1890 MPa) with satisfactory ductility for such a high-strength state (ε = 11%), but also high levels of fatigue strength, improved resistance to pitting corrosion, and enhanced in vitro biocompatibility compared to the as-received state. It was determined that the cell colonization on the 316LVM SS samples was induced by the stimulation of cell synthesis and expression of transmembrane adhesion molecules. This mechanism was primarily stimulated by the 316LVM steel samples after HPT at 20 °C. The colonization of 316LVM SS after such processing could be influenced by the surface morphology of the nanocrystalline material and its chemical composition. Both of these factors can promote or inhibit changes in the local membrane potential of the cell in the contact area, which stimulates protein synthesis and the formation of covalent bonds with the cell membrane. As a result, the increase in the concentration of membrane-bound molecules affects the formation of a tighter intercellular contact. This, in turn, enhances the effectiveness of co-stimulation, leading to an increase in the functional potential of the MMSCs. It should also be noted that the inhibition of changes in the local membrane potential of the cell may have been influenced by the segregation of Mo–Cr–Si, which resulted in a deterioration of cell colonization in the steel after HPT at 400 °C.

The obtained data suggest that the 316LVM SS after HPT at 20 °C can be considered as a material for the development of submerged implants and metal structures for osteosynthesis. These implants will effectively stimulate cell colonization on their surface and promote accelerated fixation in the area of bone defect repair, leading to the enhanced cell differentiation of pluripotent stromal cells. Additionally, they will contribute to the increase in periosteal formation and local neo-osteogenesis. The utilization of HPT processing at 20 °C will not only significantly improve the operational characteristics but also reduce the weight of medical devices. This is especially important in the development of implantable prostheses for skeletal defect replacement, as it enables a significant increase in the specific strength of the steels. Furthermore, the miniaturization of medical devices will result in a reduced negative impact on the human body from the presence of foreign implants.

5. Conclusions

1. HPT at room temperature and at 400 °C forms a nanocrystalline austenitic structure in 316LVM steel.
2. HPT at both temperatures increases the microhardness of steel by more than 2.5 times.
3. After HPT at 400 °C, the 316LVM steel is less ductile (ε = 1%) than after HPT at room temperature (ε = 11%) at the same level of strength.
4. HPT increases the endurance limit of the 316LVM steel by more than two times (up to 550 MPa) compared to the initial state. At the same time, HPT at 400 °C reduces low-cycle fatigue.
5. Nanostructuring by HPT at 400 °C worsens the corrosion resistance of steel, in contrast to HPT at 20 °C.
6. HPT at 20 °C of the 316LVM SS stimulates cell synthesis and the expression of transmembrane adhesion molecules, leading to improved cell colonization on the surface of the samples.

These results indicate the potential of nanocrystalline surgical grade 316LVM stainless steel after HPT at 20 °C for medical use. An attempt to additionally strengthen 316LVM steel by the precipitation of segregations during HPT at 400 °C was not successful. It was shown that nanostructured 316LVM steel after HPT at 400 C does not have sufficient ductility, corrosion resistance, and biocompatibility, which does not allow it to be recommended for widespread use.

Author Contributions: Conceptualization, O.R., M.K. and S.D.; methodology, N.A., N.M., G.R. and M.K.; software, G.R., A.T., D.P. and M.G.; validation, O.R., N.A. and N.M.; formal analysis, O.R. and N.M.; investigation, O.R., N.A., N.M., G.R., A.T., E.L., D.P. and M.G.; resources, A.T.; data curation, A.T., E.L. and S.D.; writing—original draft preparation, O.R. and N.A.; writing—review and editing, G.R., S.D., E.L., M.K. and N.M.; visualization, O.R., G.R., M.G., N.A. and E.L.; supervision, S.D. and M.K.; project administration, O.R.; funding acquisition, S.D. All authors have read and agreed to the published version of the manuscript.

Funding: This research was carried out with the support of the Russian Federation state assignment of A.A. Baikov Institute of Metallurgy and Materials Science of the Russian Academy of Science (IMET RAS), Russia (Theme No. 075-01176-23-00).

Data Availability Statement: All the data required to reproduce these experiments are present in the article.

Acknowledgments: The study of fractography was carried out using the research equipment of the Shared Facility Center of the P.N. Lebedev Physical Institute of RAS "Center for the Study of High-Temperature Superconductors and Other Strongly Correlated Electronic Systems".

Conflicts of Interest: The authors declare no conflict of interest.

References

1. Marshall, P. *Austenitic Stainless Steel: Microstructure and Mechanical Properties*; Elsevier Applied Science Publishers: London, UK; New York, NY, USA, 1984.
2. Davis, J.R. *Handbook of Materials for Medical Devices*; Metallic Materials; ASM International: Materials Park, OH, USA, 2003; Chapter 3.
3. Pilliar, R.M. Metallic Biomaterials. In *Biomedical Materials*; Narayan, R., Ed.; Springer: Boston, MA, USA, 2009; pp. 41–81. [CrossRef]
4. Teoh, S.H. Fatigue of biomaterials: A review. *Int. J. Fatigue* **2000**, *22*, 825–837. [CrossRef]
5. *ISO 5838-1:2013*; Implants for Surgery Metallic Skeletal Pins and Wires. Part 1: General Requirements. International Organization for Standardization: Geneva, Switzerland, 2022.
6. Kashyap, B.P.; Tangri, K. On the Hall-Petch relationship and substructural evolution in type 316L stainless steel. *Acta Metall. Mater.* **1995**, *43*, 3971–3981. [CrossRef]
7. Valiev, R.Z.; Langdon, T.G. Principles of equal-channel angular pressing as a processing tool for grain refinement. *Prog. Mater. Sci.* **2006**, *51*, 881–981. [CrossRef]
8. Zhilyaev, A.P.; Langdon, T.G. Using high-pressure torsion for metal processing: Fundamentals and applications. *Prog. Mater. Sci.* **2008**, *53*, 893–979. [CrossRef]
9. Dong, F.Y.; Zhang, P.; Pang, J.C.; Chen, D.M.; Yang, K.; Zhang, Z.F. Optimizing strength and ductility of austenitic stainless steels through equal-channel angular pressing and adding nitrogen element. *Mater. Sci. Eng. A* **2013**, *587*, 185–1917. [CrossRef]
10. Ueno, H.; Kakihata, K.; Kaneko, Y.; Hashimoto, S.; Vinogradov, A. Enhanced fatigue properties of nanostructured austenitic SUS 316L stainless steel. *Acta Mater.* **2011**, *59*, 7060–7069. [CrossRef]
11. Huang, C.X.; Yang, G.; Gao, Y.L.; Wu, S.D.; Zhang, Z.F. Influence of processing temperature on the microstructures and tensile properties of 304L stainless steel by ECAP. *Mater. Sci. Eng. A* **2008**, *485*, 643–650. [CrossRef]
12. Dobatkin, S.V.; Rybal'chenko, O.V.; Raab, G.I. Structure Formation, Phase Transformations and Properties in Cr–Ni Austenitic Steel after Equal-Channel Angular Pressing and Heating. *Mater. Sci. Eng. A* **2007**, *463*, 41–45. [CrossRef]
13. Rybalchenko, O.V.; Anisimova, N.Y.; Kiselevskiy, M.V.; Belyakov, A.N.; Tokar, A.A.; Terent'ev, V.F.; Prosvirnin, D.V.; Rybalchenko, G.V.; Raab, G.I.; Dobatkin, S.V. The influence of ultrafine-grained structure on the mechanical properties and biocompatibility of austenitic stainless steels. *J. Biomed. Mater. Res.* **2020**, *108*, 1460–1468. [CrossRef]
14. Koohdar, H.; Nili-Ahmadabadi, M.; Kalahroudi, F.J.; Jafarian, H.R.; Langdon, T.G. Effect of post-deformation annealing on the microstructure and mechanical behavior of an Fe–Ni–Mn steel processed by high-pressure torsion. *J. Mater. Res. Technol.* **2021**, *15*, 1537–1546. [CrossRef]
15. Jang, G.; Kim, J.N.; Lee, H.; Lee, T.; Enikeev, N.; Abramova, M.; Valiev, R.Z.; Kim, H.S.; Lee, C.S. Microstructural evolution and mechanical properties of nanocrystalline Fe–Mn–Al–C steel processed by high-pressure torsion. *Mater. Sci. Eng. A* **2021**, *827*, 142073. [CrossRef]
16. Biserova-Tahchieva, A.; Chatterjee, D.; van Helvoort, A.T.J.; Llorca-Isern, N.; Cabrera, J.M. Effect of the nanostructuring by high-pressure torsion process on the secondary phase precipitation in UNS S32750 Superduplex stainless steel. *Mater. Charact.* **2021**, *183*, 111639. [CrossRef]
17. Jacob, K.; Yadav, D.; Dixit, S.; Hohenwarter, A.; Jaya, B.N. High pressure torsion processing of maraging steel 250: Microstructure and mechanical behaviour evolution. *Mater. Sci. Eng. A* **2021**, *802*, 140665. [CrossRef]

18. Anijdan, S.H.M.; Koohdar, H.; Nili-Ahmadabadi, M.; Jafarian, H.R.; Langdon, T.G. Evaluation of texture weakening and microstructural evolution in an Fe–10Ni–7Mn martensitic steel severely deformed by six turns of high-pressure torsion. *Mater. Sci. Eng. A* **2022**, *851*, 143660. [CrossRef]
19. Pakieła, Z.; Garbacz, H.; Lewandowska, M.; Drużycka-Wiencek, A.; Suś-Ryszkowska, M.; Zieliński, W.; Kurzydłowski, K. Structure and properties of nanomaterials produced by severe plastic deformation. *Nukleonika* **2006**, *51*, 19–25.
20. Mine, Y.; Horita, Z.; Murakami, Y. Effect of hydrogen on martensite formation in austenitic stainless steels in high-pressure torsion. *Acta Mater.* **2009**, *57*, 2993–3002. [CrossRef]
21. Gubicza, J.; El-Tahawy, M.; Huang, Y.; Choi, H.; Choe, H.; Lábár, J.L.; Langdon, T.G. Microstructure, phase composition and hardness evolution in 316L stainless steel processed by high-pressure torsion. *Mater. Sci. Eng. A* **2016**, *657*, 215–223. [CrossRef]
22. Scheriau, S.; Zhang, Z.; Kleber, S.; Pippan, R. Deformation mechanisms of a modified 316L austenitic steel subjected to high pressure torsion. *Mater. Sci. Eng. A* **2011**, *528*, 2776–2786. [CrossRef]
23. Wang, H.; Shuro, I.; Umemoto, M.; Kuo, H.H.; Todaka, Y. Annealing behavior of nano-crystalline austenitic SUS316L produced by HPT. *Mater. Sci. Eng. A* **2012**, *556*, 906–910. [CrossRef]
24. Renk, O.; Hohenwarter, A.; Eder, K.; Kormout, K.S.; Cairney, J.M.; Pippan, R. Increasing the strength of nanocrystalline steels by annealing: Is segregation necessary? *Scr. Mater.* **2015**, *95*, 27–30. [CrossRef]
25. Renk, O.; Hohenwarter, A.; Gammer, C.; Eckert, J.; Pippan, R. Achieving 1 GPa fatigue strength in nanocrystalline 316L steel through recovery annealing. *Scr. Mater.* **2022**, *217*, 114773. [CrossRef]
26. Abramova, M.M.; Enikeev, N.A.; Valiev, R.Z.; Etienne, A.; Radiguet, B.; Ivanisenko, Y.; Sauvage, X. Grain boundary segregation induced strengthening of an ultrafine-grained austenitic stainless steel. *Mater. Lett.* **2014**, *136*, 349–352. [CrossRef]
27. Etienne, A.; Radiguet, B.; Cunningham, N.; Odette, G.; Valiev, R.; Pareige, P. Comparison of radiation-induced segregation in ultrafine-grained and conventional 316 austenitic stainless steels. *Ultramicroscopy* **2011**, *111*, 659–663. [CrossRef]
28. Dobatkin, S.V.; Rybalchenko, O.V.; Enikeev, N.A.; Tokar, A.A.; Abramova, M.M. Formation of fully austenitic ultrafine-grained high strength state in metastable Cr–Ni–Ti stainless steel by severe plastic deformation. *Mater. Lett.* **2016**, *166*, 276–279. [CrossRef]
29. Han, J.-K.; Liu, X.; Lee, I.; Kuzminova, Y.O.; Evlashin, S.A.; Liss, K.-D.; Kawasaki, M. Structural evolution during nanostructuring of additive manufactured 316L stainless steel by high-pressure torsion. *Mater. Lett.* **2021**, *302*, 130364. [CrossRef]
30. Lee, D.-H.; Gao, Z.; Park, J.-M.; Zhao, Y.; Suh, J.-Y.; Jägle, E.A.; Tsuchiya, K.; Ramamurty, U.; Jang, J. Nanomechanical and microstructural characterization on the synergetic strengthening in selectively laser melted austenitic stainless steel. *Scr. Mater.* **2022**, *209*, 114359. [CrossRef]
31. Liu, M.; Gong, W.; Zheng, R.; Li, J.; Zhang, Z.; Gao, S.; Ma, C.; Tsuji, N. Achieving excellent mechanical properties in type 316 stainless steel by tailoring grain size in homogeneously recovered or recrystallized nanostructures. *Acta Mater.* **2022**, *226*, 117629. [CrossRef]
32. *ISO 6892-1:2019*; Metallic Materials—Tensile Testing—Part 1: Method of Test at Room Temperature. International Organization for Standardization: Geneva, Switzerland, 2019.
33. *ASTM G59-23*; Standard Test Method for Conducting Potentiodynamic Polarization Resistance Measurements. ASTM International: West Conshohocken, PA, USA, 2023.
34. Choudhary, R.; Venkatraman, S.K.; Bulygina, I.; Senatov, F.; Kaloshkin, S.; Anisimova, N.; Kiselevskiy, M.; Knyazeva, M.; Kukui, D.; Walther, F.; et al. Biomineralization, dissolution and cellular studies of silicate bioceramics prepared from eggshell and rice husk. *Mater. Sci. Eng. C* **2021**, *118*, 111456. [CrossRef]
35. Anisimova, N.; Kiselevskiy, M.; Martynenko, N.; Straumal, B.; Willumeit-Römer, R.; Dobatkin, S.; Estrin, Y. Cytotoxicity of biodegradable magnesium alloy WE43 to tumor cells in vitro: Bioresorbable implants with antitumor activity? *J. Biomed. Mater. Res. B Appl. Biomater.* **2020**, *108*, 167–173. [CrossRef]
36. Yagodkin, Y.D.; Dobatkin, S.V. Application of electron microscopy and X-ray structural analysis for the determination of sizes of structural elements in nanocrystalline materials (review). *Inorg. Mater.* **2008**, *44*, 1520–1530. [CrossRef]
37. *ASTM F756-17*; Standard Practice for Assessment of Hemolytic Properties of Materials. ASTM International: West Conshohocken, PA, USA, 2017.
38. *ISO/DIS 5832-1*; Implants for Surgery Metallic Materials. Part 1: Wrought Stainless Steel. International Organization for Standardization: Geneva, Switzerland, 2016.